Electronic materials

Electrical transport properties of Weyl semimetal WTe$_2$ under high pressure

Yuqiang Li[1,3,*] , Jingxia Liu[1], Peiguang Zhang[2], Jianxin Zhang[1], Ningru Xiao[1], Liyuan Yu[1], and Pingjuan Niu[1,3,*]

[1] *Engineering Research Center of High Power Solid State Lighting Application System of Ministry of Education, Tiangong University, Tianjin 300387, China*

[2] *State Key Laboratory of Applied Optics, Changchun Institute of Optics, Fine Mechanics and Physics (CIOMP), Chinese Academy of Sciences, Changchun 130033, China*

[3] *School of Electronics and Information Engineering, Tiangong University, Tianjin 300387, China*

ABSTRACT

Tungsten ditelluride (WTe$_2$) has recently become one of the most extensively investigated materials as a Weyl semimetal with an orthorhombic T_d phase due to its unique properties, including its pressure-induced superconductivity and unsaturated giant magnetoresistance. The electrical resistivity, photoconductivity, and Hall effect under high pressures are considered in WTe$_2$ using in situ measurements up to 40 GPa. The structural phase transition is reflected from the T_d to $1T'$ phase at approximately 11 GPa based on the discontinuous electrical parameters. The abrupt increase of resistivity is caused by a joint decrease in the carrier concentration and mobility. The semimetal-to-semiconductor transition is apparent at around 11 GPa based on the resistivity measurements under different temperatures, and the transition is reversible due to the structural phase transition. The photoconductivity is much higher than the conductivity, and the phase transition pressure is lower at approximately 9.6 GPa.

Address correspondence to E-mail: liyuqiang@tiangong.edu.cn; niupingjuan@tiangong.edu.cn

Springer

GRAPHIC ABSTRACT

Electrical transport properties of Weyl Semimetal WTe$_2$ are investigated under high pressure, and pressure-induced semiconductor transition is confirmed.
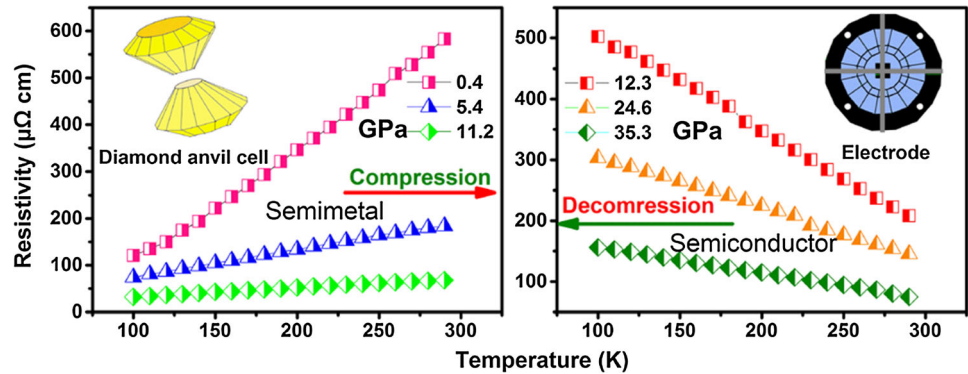
Introduction

The Weyl semimetal is a topological state characterized by Weyl points near the Fermi energy [1–3]. WTe$_2$ (chemical formula of Tungsten ditelluride) is strongly confirmed as a type-II topological Weyl semimetal [4], where the Weyl points occur at the crossing of the oblique conduction and valance bands. The Weyl semimetal WTe$_2$ represents a rare example of a material with both superconductivity under extreme conditions and a topologically nontrivial band structure [5–8]. WTe$_2$ attracts special attention for its significant physical attribute of an unsaturated giant magnetoresistance [9], which has not only been extensively applied in the field of magnetic sensors [10], magnetic memory [11], and hard drives [12] at room temperature, but their rarity has also inspired fundamental studies of material physics at low temperatures [13, 14].

High pressure has been proven to be a clean and powerful tool to modify the physical properties for various transition metal dichalcogenides [15–18]. The diamond anvil cell (DAC) is a device that generates high pressure and has been widely used to study electronic structures, optical properties, and metal–semiconductor transitions for bulk materials and nanocrystals [19–22]. This technique can also adjust the electronic band structure and accurately identify the superconductivity properties of the Weyl semimetal WTe$_2$. Kang et al. [5] reported the suppression of the large magnetoresistance and the occurrence of superconductivity in WTe$_2$ under high pressure, and the superconductivity appeared at a critical pressure of 10.5 GPa when the positive large magnetoresistance effect was turned off. The superconductivity was also observed by Pan et al. [6] sharply at 2.5 GPa, and the maximum critical temperature (Tc), which reached 7 K near 16.8 GPa, decreased monotonically with pressure, showing a typical dome-shaped superconducting phase.

It was found that the Weyl semimetal WTe$_2$ experienced a structural phase transition from T_d (Pnm21, No. 31) to $1T'$ (P21/m, No. 11) beginning at 6.0 GPa and ending at 15.5 GPa, and the zero resistance phenomenon disappeared in the phase transition pressure range but recovered after the phase transition [23]. The occurrence of pressure-induced superconductivity was caused by the structural phase transition of T_d to $1T'$ at around 4–5 GPa for WTe$_2$, which is related to a change in the Te–Te interlayer distance due to slip between the WTe$_2$ layers and the discontinuity of the Raman bands above 11 GPa [24]. The structure of the orthorhombic T_d phase for WTe$_2$ was unstable based on the results of Xia et al. [25], and the structural phase transition from the T_d phase to the monoclinic T' phase occurred at 10 GPa. At the same time, the Weyl semimetal states disappeared and the new T' phase exhibited superconducting properties.

The electrical transport properties of the Weyl semimetal WTe_2 are investigated using in situ electrical resistivity measurements and Hall effect techniques in a DAC at pressures up to 40 GPa. The semimetal-to-semiconductor transition was found at 11 GPa based on the temperature-induced resistivity, and an abrupt change in the electrical parameters was related to the pressure-induced phase transition. Experimental evidence for the photoconductivity with pressure is lacking, though this is of fundamental importance. Therefore, the pressure-driven photoconductivity is considered for WTe_2 here. The abrupt change in photoconductivity is related primarily to the semimetal to semiconductor transition, and the photoconductivity is higher than the conductivity for WTe_2 as it results from photogenerated carriers.

Experimental section

The experimental sample was ground WTe_2 powder obtained from 2D Semiconductors Company with a purity of 99.9999%. The initial structure of the sample was the T_d phase as a Weyl semimetal, which is similar to a previous report based on in situ Raman measurements [24]. The high pressure was generated with a non-magnetic DAC for the in situ Hall effect and resistivity measurements. The anvil culet was 300 μm in diameter with a bevel angle of 10°. A rhenium sheet was pre-indented to be 60 μm thick as the gasket for the Hall effect measurements, and a 120-μm-diameter hole was drilled in the center of the indentation using laser drilling. A similar T301 stainless steel gasket was applied for the temperature-dependent resistivity measurements. A mixture of diamond powder, glue, and polymethylmethacrylate (PMMA) was compressed into the indentation area of the gasket as an insulating layer between the probing electrodes and metallic gasket, and an 80-μm-diameter hole was drilled in the center as the sample chamber.

The details of the manufacturing processes and configuration of the insulating gasket are reported in a previous paper [26]. A standard K-type thermocouple was used to measure the temperature at the side face of the diamond anvil. There was no pressure-transmitting medium to avoid additional errors in the electrical parameter measurements, and the sample chamber was filled with compacted WTe_2. A
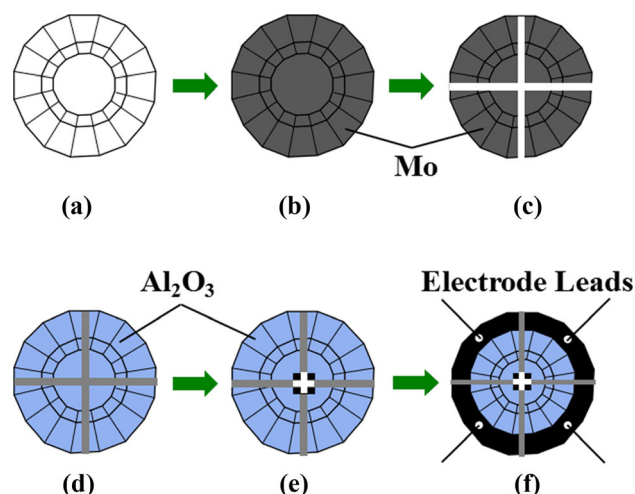

Figure 1 Manufacturing process for the integrated microcircuit on a diamond anvil: **a** clean diamond, **b** Mo thin film sputtered on the diamond anvil, **c** crisscross Mo thin film removed via photolithography, **d** Al_2O_3 thin film sputtered as an insulating layer, **e** square Al_2O_3 thin film removed via photolithography, and **f** configuration of a complete microcircuit after removing the Al_2O_3 from the electrode leads.

small ruby ball for pressure calibration was loaded into the sample chamber for the high-pressure electrical measurements [27, 28]. The thickness of the sample at high pressures was measured with an electronic micrometer [29]. Four molybdenum electrodes were arranged to contact the sample in the chamber as combined with magnetron sputtering and photolithography. The manufacturing process for the integrated microcircuit is shown in Fig. 1a–f. Enameled wire was used as electrical leads in Fig. 1f, and the enameled wire was made of copper core and insulating lacquer. The copper core of 100 μm diameter was connected with metal molybdenum electrode after removing insulating lacquer, and the copper core was fixed with molybdenum of side diamond by drying and curing conductive silver paste. The associated experimental parameters are shown in Tables S1(a)–S1(c) in the Supplementary Information. The integration process of the microcircuit is the same as previous works [30, 31].

The resistivity and Hall effect experiments were performed using the van der Pauw method. The current and the voltage were detected with a Keithley 2400 source meter and Keithley 2700 multimeter, respectively. The uniform magnetic field was generated with an EM7 electromagnet from East Changing Company, and a Lakeshore model 420 Gauss meter

was applied to measure the magnetic field. The photoconductivity measurements were performed using a laser with a wavelength of 532 nm and a power restricted to < 5 mW to limit thermal damage to the sample. A fixed laser exposure time of 20 s was used throughout the photoconductivity experiments.

Results and discussion

The pressure-dependent electrical parameters for WTe$_2$ are shown in Fig. 2 for the Hall coefficient R_H, carrier concentration n, mobility μ, and resistivity ρ. At larger pressures, R_H and ρ both show decreasing trends and have a sharp increase above 11.2 GPa in Fig. 2a, d, respectively. Conversely, n and μ both have increasing trends with pressure until there is a sudden decrease at approximately 11.2 GPa in Fig. 2b, c, respectively. The abrupt changes in the above parameters are attributed to the structural phase transition from T_d to the monoclinic $1T'$ phase. The discontinuous electrical parameters are consistent with the phase transition pressure zone beginning at 6.0 GPa and ending at 15.5 GPa based on synchrotron X-ray diffraction [23]. This structural phase transition has also been reported above 11 GPa based on the discontinuity of Raman bands [24] and

proven above 10 GPa by Raman microspectroscopy and ab initio calculations [25]. The structural phase transition causes atomic rearrangement and changes in the electronic structure, which lead to the abnormal electrical parameters. T_d phase WTe$_2$ crystallizes in the orthorhombic structure with a distorted octahedral coordination, which is uniquely different from the typical monoclinic structure in $1T'$ phase WTe$_2$. The tungsten atoms are sandwiched between two layers of tellurium atoms in which one layer is rotated 180° in the T_d phase forming the W-Te$_6$ octahedral coordination, these layers in the T_d and $1T'$ phase exhibit buckled surface structure, and the $1T'$ structure is very similar to T_d such that it can be constructed from the T_d phase with shear strain which introduces an inversion center [24]. Due to the similarity between the T_d and $1T'$ structure, the transition path can be simply considered using an applied shear strain along the b axis. Compared with T_d phase, $1T'$ phase undergoes an opposite sliding within adjacent layers leading to the unit cell change from orthorhombic to monoclinic symmetry [25]. In $1T'$ phase, there are three bands near the Fermi level, two electron-like bands and one hole-like band, composing the Fermi surface. The band structures and the Fermi surface of the $1T'$ phase are very similar to

Figure 2 Pressure dependence of the **a** Hall coefficient R_H, **b** carrier concentration n, **c** mobility μ, and **d** resistivity ρ for WTe$_2$ (dashed line indicates the transition pressure of the two phases).
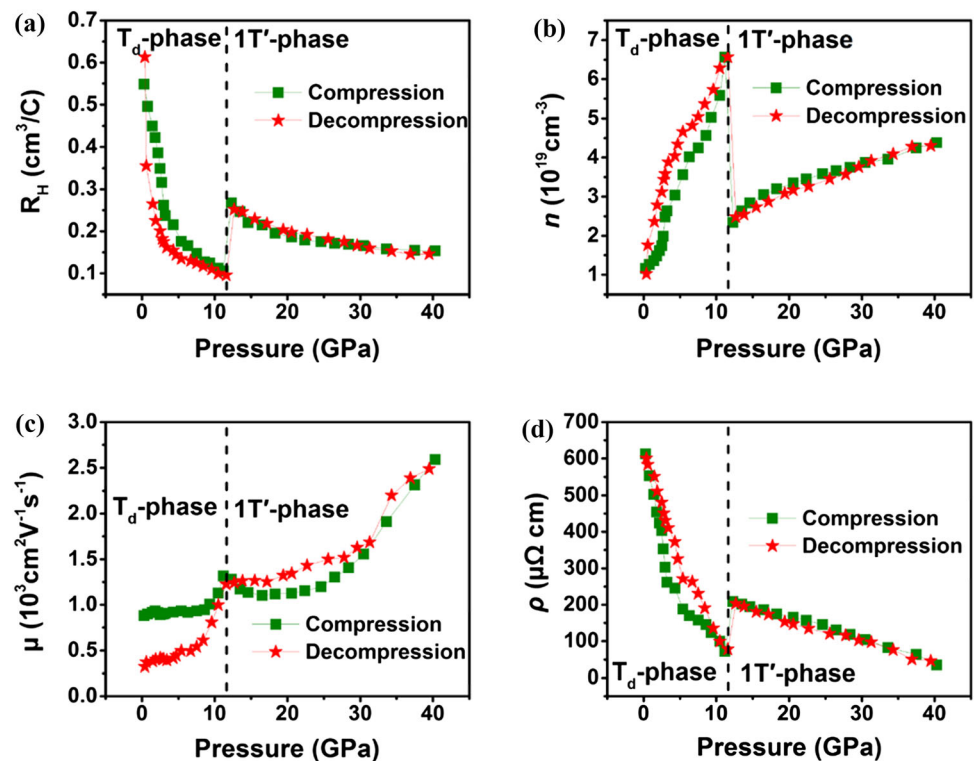
those in the T_d phase [9], including a perfect balance between electron and hole pockets. Application of pressure is an efficient method to tune the lattice constants and thereby atomic interactions, which has been reported to produce new phases of materials [32]. In the T_d phase, spin degeneracy is broken by the spin-orbital coupling due to the absence of an inversion symmetry, while the spin degeneracy will remain in the $1T'$ phase; therefore, the Weyl fermions in the ambient T_d phase should disappear after the structure phase transition [24]. Thus, the abrupt change in the electrical parameters reflects the structural phase transition for the Weyl semimetal WTe_2 from T_d to $1T'$ at approximately 11.2 GPa.

The Hall effect can be analyzed from the average motion of multiple scatterings, where the carriers move freely in the electromagnetic field between scattering events. The motion of an electron in an electromagnetic field consists of two parts: motion from the initial velocity v_0 under the magnetic field and motion with an initial velocity of zero under the electric and magnetic fields. The first part is a spiral motion with the magnetic field direction as the axis, which is the superposition of the uniform motion along the magnetic field and the circular motion perpendicular to the magnetic field. Their regular motion that occurs after each scattering indicates that the average motion from scattering should be zero after multiple scattering events. Therefore, it is only necessary to analyze the second motion, which is the initial velocity of zero between each scattering. The associated equation is given by

$$R_H = -\frac{1}{nq}\frac{\langle \tau^2 v^2 \rangle \langle v^2 \rangle}{\langle \tau v^2 \rangle^2} \quad (1)$$

where τ is the average free time, v is the carrier velocity, q is the electronic charge, and $\langle\ \rangle$ represents the statistical average. Ignoring the effects of statistical averages, Eq. (1) is simplified to the following form.

$$R_H = -\frac{1}{nq} \quad (2)$$

The R_H and n for WTe_2 satisfy the above equations regardless of their sign under high pressures. The R_H exhibits a sudden increase at approximately 11.2 GPa in Fig. 2a, while the n has an abrupt decrease in Fig. 2b. An increase of R_H is attributed to a decrease of n at approximately 11.2 GPa based on Eq. (2). The

carrier mobility and electrical conductivity are obtained by calculating the average drift velocity from the external electric field. The average drift velocities for electrons and holes are not the same. The average drift velocity of the conduction band electron is larger and the mobility of electrons is greater than for holes. The expression for the total current density J is:

$$J = J_n + J_p = (nq\mu_n + pq\mu_p)\varepsilon \quad (3)$$

where μ_n and μ_p represent the electron and hole mobilities, respectively, J_n and J_p are the electron and hole current densities, respectively, n and p represent the concentrations of electrons and holes, respectively, and ε is the electric field strength.

When the electric field is moderate, the relationship (4) between J and the conductivity σ still follows Ohm's law [Eq. (4)], while σ can be obtained from Eq. (5). For impurity semiconductors whose concentrations differ widely between carriers and whose mobilities vary little, their conductivity depends on the carrier majority. The resistivity and conductivity are as shown in Eq. (6). For n-type semiconductors, the electrons are the majority carrier, and the holes are the minority carrier, $n \gg p$, the contribution of holes to the current is negligible comparing with electrons. The n and μ_n both show an abrupt decrease around 11.2 GPa in Fig. 2b, c, respectively, while ρ has a strong increase in Fig. 2d, which is due to the mutual reduction of the carrier concentration and mobility. The electrical parameters are reassigned their initial states after releasing the pressure to ambient in Fig. 2, which indicates the structural phase transition is also reversible for the Weyl semimetal WTe_2 from T_d to $1T'$.

$$J = \sigma\varepsilon \quad (4)$$

$$\sigma = nq\mu_n + pq\mu_p \quad (5)$$

$$\rho = \frac{1}{\sigma} = \frac{1}{nq\mu_n} \quad (6)$$

To further reveal the effects of pressure on the electrical transport properties, we perform temperature-dependent measurements of the resistivity in the Weyl semimetal WTe_2 at different pressures. The pressure evolutions for the temperature dependencies of resistivity (ρ-T curves) are shown in Fig. 3a, b for the T_d and $1T'$ phases, respectively. The semimetal nature at lower pressures is characterized by the thermal activation type conduction at low
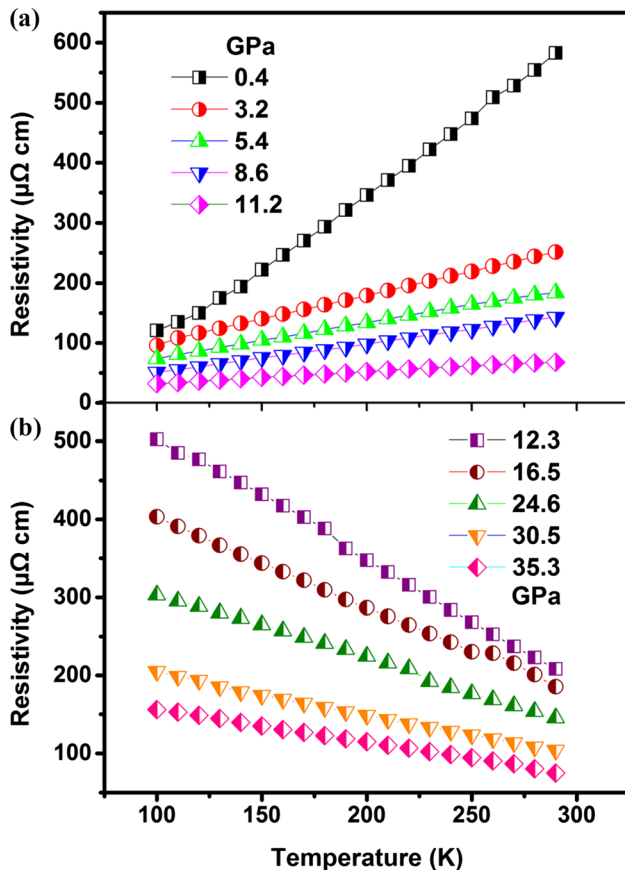
Figure 3 Resistivity-temperature curves under several pressures for **a** T_d phase and **b** $1T'$ phase.

suggests that the T_d to $1T'$ transition occurred with the vanishing $P3$ band and the occurrence of the $P4$ band with a higher frequency. The Raman peaks at approximately 120 cm^{-1} gradually softened after increasing the pressure and were completely suppressed above 10 GPa, indicating the phase transitioned from T_d to $1T'$ [25]. For semiconductors, the resistivity is determined primarily from the intrinsic carrier concentration. With increasing temperature, the carrier concentration increases, and the mobility slightly decreases, which leads to a smaller resistivity. The resistivity of semiconductors decreases monotonically with temperature, which is an important characteristic of semiconductors and distinguishes them from semimetals [34–36].

Below 11.2 GPa in Fig. 3a, the resistivity–temperature slope ($d\rho/dT$) clearly shows semimetallic characteristics with a positive temperature dependence. The slope indicates the variation of resistivity per unit temperature range reflecting changes of carrier concentration and mobility with temperature. For pressures above 12.3 GPa in Fig. 3b, there is a significant increase in the electrical resistivity, and the curves have a negative slope ($d\rho/dT$), which is characteristic of semiconductors. The semiconducting characteristics are then maintained up to 35.3 GPa. The pressure evolutions of the resistance–temperature dependencies are exhibited in Figs. S1(a) and S1(b) in the Supplementary Information. The resistance–temperature slope (dR/dT) clearly shows reversibility, suggesting the semimetal-to-semiconductor transition is reversible.

High-pressure photoconductivity measurements were performed under green light illumination at a wavelength of $\lambda = 532$ nm in a DAC up to 30 GPa. Figure 4 shows the conductivity and photoconductivity of WTe$_2$ under compression and decompression conditions. The photoconductivity is defined here as conductivity under green light illumination. As shown in Fig. 4a, photoconductivity and conductivity both increase with pressure before an abrupt decrease at 9.6 and 11.4 GPa, respectively, and then continue increasing at higher applied pressures. During compression, the photoconductivity is much higher than the conductivity before 9.6 and after 11.4 GPa. In Fig. 4b, the photoconductivity and conductivity in the decompression zone both have similar discontinuous phenomena at the vicinity of 9.6 and 11.4 GPa, respectively, and the photoconductivity is much higher than at a similar pressure zone
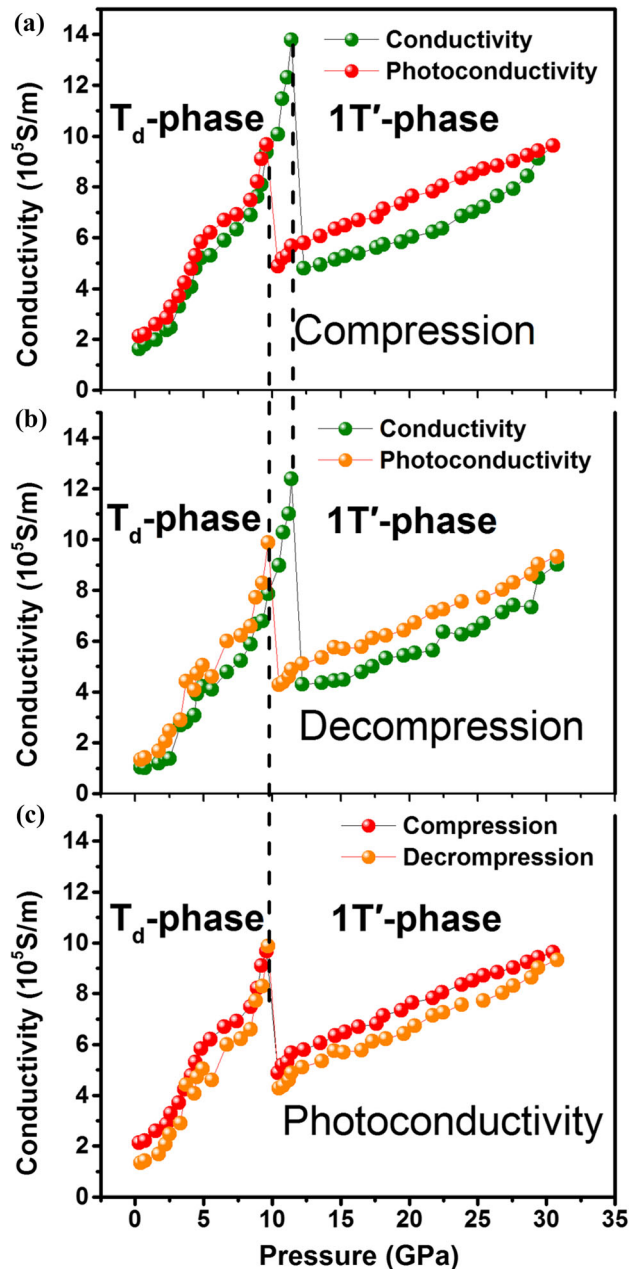
temperatures and is gradually suppressed at higher pressures. The ρ-T curves when under a few GPa transform into the non-thermal activation type. At higher pressures, the resistivity shows an increasing trend from ambient to 11.2 GPa in Fig. 3a but decreases with pressure from 11.2 to 35.3 GPa in Fig. 3b. This suggests a kind of semimetal-to-semiconductor transition in the Weyl semimetal WTe$_2$, which is believed to be driven by a reduced overlap of the semimetal conduction and valence bands, while the Fermi surfaces shrink and eventually vanish as the overlap decreases [33].

The pressure-induced semimetal-to-semiconductor transition is also caused by the structural phase transition at around 11 GPa. There is a related discussion on the issue of the pressure-induced phase transition based on Raman measurements. The occurrence of the structural phase transition had been previously confirmed at approximately 11 GPa using high-pressure Raman measurements [24]. The discontinuity of Raman bands above 11 GPa also

Figure 4 Conductivity and photoconductivity of WTe_2 under **a** compression and **b** decompression conditions, and **c** the photoconductivity of WTe_2 under compression and decompression conditions.

under compression. These discontinuous changes are due to the semimetal-to-semiconductor phase change caused by the structural phase transition at approximately 11 GPa.

Light absorption causes the formation of non-equilibrium carriers in WTe_2, and the increased carrier concentration gives a larger sample conductivity. The concentrations of the non-equilibrium carriers

are Δn and Δp when injected with light, respectively. When the electrons are initially excited to the conduction band, they may possess more energy than the thermal equilibrium electrons. This is because the photogenerated electrons lose excess energy in the form of emission in a relatively short time by colliding with the lattice during thermal equilibrium. Therefore, the photogenerated electrons and the thermal equilibrium electrons have the same mobility during the entire photoconductivity process. The additional photoconductivity can be written as:

$$\Delta \sigma = \Delta n q \mu_n + \Delta p q \mu_p \tag{7}$$

For many semiconductor materials, it has been confirmed that $\Delta n = \Delta p$ for intrinsic absorption, but photogenerated electrons and holes do not both contribute to the photoconductivity. The intrinsic photoconductivity is due primarily to the existence of photogenerated holes (p-type) or electrons (n-type). This suggests that while the number of light-excited electrons and holes is equal in the intrinsic photoconductivity, only one of the carriers exists in the unconstrained state over a long period before their recombination disappears, while the other carrier is often bound by certain energy levels [37–39].

In addition to the intrinsic photoconductivity, light also enables the ionization of electrons or holes bound to the impurity levels to produce impurity photoconductivity. However, as the number of impurity atoms is much smaller than the number of atoms in the crystal itself for powder sample with purity of 99.9999%, the impurity photoconductivity is relatively weak. Nevertheless, impurity absorption and photoconductivity are important methods to study the sample impurity levels. Therefore, photoconductivity is higher than the conductivity for WTe_2. The photoconductivity of WTe_2 is given in Fig. 4c under compression and decompression conditions. The discontinuous photoconductivity is observed around 9.6 GPa, which is lower than the 11.4 GPa for conductivity. This shows that the light reduces the pressure of the phase transition. The photoconductivity also returns to its initial state after releasing from high pressure to ambient conditions, which indicates the semimetal-to-semiconductor phase transition is reversible. This may provide a potential way to reduce the phase transition pressure of such transitions.

Conclusions

The discontinuous electrical parameters reflect the structural phase transition of the Weyl semimetal WTe_2 from the T_d to the $1T'$ phase. The abnormal increase of R_H is caused by a decrease of n at approximately 11.2 GPa, while resistivity is due to the combined decrease of the carrier concentration and mobility. The transition is confirmed from semimetal-to-semiconductor at around 11 GPa based on the temperature-dependent resistivity, while the decompression electrical parameters indicate the transition is reversible. The semimetal-to-semiconductor transition is caused by the structural phase transition. The photoconductivity is much higher than the conductivity, and the phase transition pressure is lower at approximately 9.6 GPa under illumination. The results may provide a potential way to switch the transition pressure of the Weyl semimetal-to-semiconductor transition for a given material using lasers under high pressure.

Supplementary material

Related experimental parameters are shown, and the pressure evolution of the temperature-dependent resistance is exhibited. This material is available free of charge via the Internet.

Acknowledgements

Compliance with ethical standards

Conflict of interest   There are no conflicts of interest to declare.

Electronic supplementary material: The online version of this article (https://doi.org/10.1007/s108 53-020-05045-z) contains supplementary material, which is available to authorized users.

References

[1] Zhang Y, Sun Y, Yan B (2018) Berry curvature dipole in Weyl semimetal materials: an ab initio study. Phys Rev B 97:041101

[2] Burkov AA, Hook MD, Balents L (2011) Topological nodal semimetals. Phys Rev B 84:235126

[3] Wan X, Turner AM, Vishwanath A, Savrasov SY (2011) Topological semimetal and Fermi-arc surface states in the electronic structure of pyrochlore iridates. Phys Rev B 83:205101

[4] Li P, Wen Y, He X, Zhang Q, Xia C, Yu Z, Yang SA, Zhu Z, Alshareef HN, Zhang X (2017) Evidence for topological type-II Weyl semimetal WTe_2. Nat Commun 8:2150

[5] Kang D, Zhou Y, Yi W, Yang C, Guo J, Shi Y, Zhang S, Wang Z, Zhang C, Jiang S, Li A, Yang K, Wu Q, Zhang G, Sun L, Zhao Z (2015) Superconductivity emerging from a suppressed large magnetoresistant state in tungsten ditelluride. Nat Commun 6:7804

[6] Pan X, Chen X, Liu H, Feng Y, Wei Z, Zhou Y, Chi Z, Pi L, Yen F, Song F, Wan X, Yang Z, Wang B, Wang G, Zhang Y (2015) Pressure-driven dome-shaped superconductivity and electronic structural evolution in tungsten ditelluride. Nat Commun 6:7805

[7] Sante DD, Das PK, Bigi C, Ergönenc Z, Gürtler N, Krieger JA, Schmitt T, Ali MN, Rossi G, Thomale R, Franchini C, Picozzi S, Fujii J, Strocov VN, Sangiovanni G, Vobornik I, Cava RJ, Panaccione G (2017) Three-dimensional electronic structure of the type-II Weyl semimetal WTe_2. Phys Rev Lett 119:026403

[8] Yu P, Fu W, Zeng Q, Lin J, Yan C, Lai Z, Tang B, Suenaga K, Zhang H, Liu Z (2017) Controllable synthesis of atomically thin type-II Weyl semimetal WTe_2 nanosheets: an advanced electrode material for all-solid-state flexible supercapacitors. Adv Mater 29:1701909

[9] Ali MN, Xiong J, Flynn S, Tao J, Gibson QD, Schoop LM, Liang T, Haldolaarachchige N, Hirschberger M, Ong NP, Cava RJ (2014) Large, non-saturating magnetoresistance in WTe_2. Nature 514:205–208

[10] El-Ahmar S, Koczorowski W, Poźniak AA, Kuświk P, Przychodnia M, Dembowiak J, Strupiński W (2019) Planar configuration of extraordinary magnetoresistance for 2D-material-based magnetic field sensors. Sensor Actuator A Phys 296:249–253

[11] Moritomo Y, Asamitsu A, Kuwahara H, Tokura Y (1996) Giant magnetoresistance of manganese oxides with a layered perovskite structure. Nature 380:141–144

[12] Daughton JM (1999) GMR applications. J Magn Magn Mater 192:334–342

[13] Urushibara A, Moritomo Y, Arima T, Asamitsu A, Kido G, Tokura Y (1995) Insulator-metal transition and giant magnetoresistance in $La_{1-x}Sr_xMnO3$. Phys Rev B 51:14103–14109

[14] Jo NH, Wang L, Orth PP, Bud'ko SL, Canfield PC (2019) Magnetoelastoresistance in WTe_2: exploring electronic structure and extremely large magnetoresistance under strain. Proc Natl Acad Sci USA 116:25524–25529

[15] Chi Z, Zhao X, Zhang H, Goncharov AF, Lobanov SS, Kagayama T, Sakata M, Chen X (2014) Pressure-induced metallization of molybdenum disulfide. Phys Rev Lett 113:036802

[16] Dou X, Ding K, Jiang D, Sun B (2014) Tuning and identification of interband transitions in monolayer and bilayer molybdenum disulfide using hydrostatic pressure. ACS Nano 8:7458–7464

[17] Zhao Z, Zhang H, Yuan H, Wang S, Lin Y, Zeng Q, Xu G, Liu Z, Solanki GK, Patel KD, Cui Y, Hwang HY, Mao WL (2015) Pressure induced metallization with absence of structural transition in layered molybdenum diselenide. Nat Commun 6:7312

[18] Nayak AP, Pandey T, Voiry D, Liu J, Moran ST, Sharma A, Tan C, Chen C, Li L, Chhowalla M, Lin J, Singh AK, Akinwande D (2015) Pressure-dependent optical and vibrational properties of monolayer molybdenum disulfide. Nano Lett 15:346–353

[19] Lyapin SG, Itskevich IE, Trojan IA, Klipstein PC, Polimeni A, Eaves L, Main PC, Henini M (1999) Pressure-induced Γ-X crossover in self-assembled In(Ga)As/GaAs quantum dots. Phys Status Solidi B 211:79–83

[20] Bassett WA (2009) Diamond anvil cell, 50th birthday. High Press Res 29:163–186

[21] Nicolle J, Machon D, Poncharal P, Pierre-Louis O, San-Miguel A (2001) Pressure-mediated doping in graphene. Nano Lett 11:3564–3568

[22] Zhou PY, Dou XM, Wu XF, Ding K, Li MF, Ni HQ, Niu ZC, Jiang DS, Sun BQ (2014) Single-photon property characterization of 1.3 μm emissions from InAs/GaAs quantum dots using silicon avalanche photodiodes. Sci Rep 4:3633

[23] Zhou Y, Chen X, Li N, Zhang R, Wang X, An C, Zhou Y, Pan X, Song F, Wang B, Yang W, Yang Z, Zhang Y (2016) Pressure-induced Td to 1T′ structural phase transition in WTe_2. AIP Adv 6:075008

[24] Lu P, Kim J, Yang J, Gao H, Wu J, Shao D, Li B, Zhou D, Sun J, Akinwande D, Xing D, Lin J (2016) Origin of superconductivity in the Weyl semimetal WTe_2 under pressure. Phys Rev B 94:224512

[25] Xia J, Li D, Zhou J, Yu P, Lin J, Kuo J, Li H, Liu Z, Yan J, Shen Z (2017) Pressure-induced phase transition in Weyl semimetallic WTe_2. Small 13:1701887

[26] Li Y, Gao Y, Han Y, Liu C, Ren W, Wang Q, Ma Y, Wu B, Gao C (2012) Electrical transport properties of $BaWO_4$ under high pressure. J Phys Chem C 116:25198–25205

[27] Mao HK, Xu J, Bell PM (1986) Calibration of the ruby pressure gauge to 800 kbar under quasi-hydrostatic conditions. J Geophys Res Solid Earth 91:4673–4676

[28] Piermarini GJ, Block S, Barnett JD, Forman RA (1975) Calibration of the pressure dependence of the R1 ruby fluorescence line to 195 kbar. J Appl Phys 46:2774–2780

[29] Li M, Gao C, Peng G, He C, Hao A, Huang X, Zhang D, Yu C, Ma Y, Zou G (2007) Thickness measurement of sample in diamond anvil cell. Rev Sci Instrum 78:075106

[30] Li Y, Gao Y, Han Y, Wang Q, Li Y, Su N, Zhang J, Liu C, Ma Y, Gao C (2012) High-pressure electrical transport behavior in WO_3. J Phys Chem C 116:5209–5214

[31] Han Y, Gao C, Ma Y, Liu H, Pan Y, Luo J, Li M, He C, Huang X, Zou G, Li Y, Li X, Liu J (2005) Integrated microcircuit on a diamond anvil for high-pressure electrical resistivity measurement. Appl Phys Lett 86:064104

[32] Zhou Y, Lu P, Du Y, Zhu X, Zhang G, Zhang R, Shao D, Chen X, Wang X, Tian M, Sun J, Wan X, Yang Z, Yang W, Zhang Y, Xing D (2016) Pressure-induced new topological Weyl semimetal phase in TaAs. Phys Rev Lett 117:146402

[33] Armitage NP, Tediosi R, Lévy F, Giannini E, Forro L, van der Marel D (2010) Infrared conductivity of elemental bismuth under pressure: evidence for an avoided lifshitz-type semimetal-semiconductor transition. Phys Rev Lett 104:237401

[34] Matsuoka T, Shimizu K (2009) Direct observation of a pressure-induced metal-to-semiconductor transition in lithium. Nature 458:186–189

[35] Enderlein C, Ramos SM, Bittencourt M, Continentino MA, Brewer W, Baggio-Saitovich E (2013) Anomaly close to an electronic topological semimetal-insulator transition in elemental fcc-Yb under pressure. J Appl Phys 114:143711

[36] Cui H, Brooks JS, Kobayashi A, Kobayashi H (2009) Metallization of the single component molecular semiconductor $[Ni(ptdt)_2]$ under very high pressure. J Am Chem Soc 131:6358–6359

[37] Zhang S, Shi J, Chen Y, Huo Q, Li W, Wu Y, Sun Y, Zhang Y, Wang X, Jiang Z (2020) Unraveling and manipulating of NADH oxidation by photogenerated holes. ACS Catal 10:4967–4972

[38] Gao C, Yu H, Zhang L, Zhao Y, Xie J, Li C, Cui K, Yu J (2020) Ultrasensitive paper-based photoelectrochemical sensing platform enabled by the polar charge carriers-created electric field. Anal Chem 92:2902–2906

[39] Rahman S, Samanta S, Kuzmin A, Errandonea D, Saqib H, Brewe DL, Kim J, Lu J, Wang L (2019) Tuning the photoresponse of nano-heterojunction: pressure-induced inverse photoconductance in functionalized WO_3 nanocuboids. Adv Sci 6:1901132

Publisher's Note Springer Nature remains neutral with regard to jurisdictional claims in published maps and institutional affiliations.